Electrical control of spatial resolution in mixed-dimensional heterostructured photodetectors

Ke Zhang[a], Yang Wei[a,1], Jin Zhang[a], He Ma[b], Xinhe Yang[a], Gaotian Lu[a], Kenan Zhang[a], Qunqing Li[a], Kaili Jiang[a,c], and Shoushan Fan[a,c]

[a]State Key Laboratory of Low-Dimensional Quantum Physics, Department of Physics and Tsinghua-Foxconn Nanotechnology Research Center, Tsinghua University, Beijing 100084, China; [b]College of Applied Science, Beijing University of Technology, Beijing 100124, China; and [c]Collaborative Innovation Center of Quantum Matter, Beijing 100084, China

Edited by Hongjie Dai, Department of Chemistry, Stanford University, Stanford, CA, and approved February 25, 2019 (received for review October 6, 2018)

Low-dimensional nanomaterials, such as one-dimensional (1D) nanomaterials and layered 2D materials, have exhibited significance for their respective unique electronic and optoelectronic properties. Here we show that a mixed-dimensional heterostructure with building blocks from multiple dimensions will present a synergistic effect on photodetection. A carbon nanotube (CNT)–WSe_2–graphene photodetector is representative on this issue. Its spatial resolution can be electrically switched between high-resolution mode (HRM) and low-resolution mode (LRM) revealed by scanning photocurrent microscopy (SPCM). The reconfigurable spatial resolution can be attributed to the asymmetric geometry and the gate-tunable Fermi levels of these low-dimensional materials. Significantly, an interference fringe with 334 nm in period was successfully discriminated by the device working at HRM, confirming the efficient electrical control. Electrical control of spatial resolution in CNT–WSe_2–graphene devices reveals the potential of the mixed-dimensional architectures in future nanoelectronics and nano-optoelectronics.

2D materials | carbon nanotubes | van der Waals heterostructures | electrical control | photodetectors

New low-dimensional nanomaterials with unique properties are constantly emerging, which greatly promotes the development of nanoelectronics (1–5) and nano-optoelectronics (6–12). A variety of van der Waals (vdW) heterostructures have been developed on the basis of 2D nanomaterials by simple stacking procedures, due to their atomically smooth surface and the 2D geometry (13–15). It is prospective to construct photodetectors on such vdW heterostructures, as the vertically stacked architecture and atomic thickness are much more efficient for charge separation and transport (16–19). Moreover, many new nanodevices were fabricated on the vertical dimension by this methodology, such as field-effect transistors (FETs) (20, 21), memories (22–24), etc. Recently, the field of nanodevices has made important advancements beyond the conventional devices, because of the employment of hybrid architectures with multiple low-dimensional nanomaterials. By using the one-dimensional (1D) nanostructure of a single-walled carbon nanotube (SWCNT), a 1D2D-FET with a MoS_2 channel and a SWCNT gate accessed a 1-nm physical gate length, which provides insight into the ultimate scaling of gate lengths for FETs (25). In addition, a graphene-contacted carbon nanotube (CNT) FET with channel length of 5 nm can operate much faster at a much lower supply voltage with a much smaller subthreshold slope (26). Vertical point heterostructures of SWCNT–MoS_2–SWCNT greatly reduced the FET area (27). These achievements suggest that it is an essential issue to integrate functional nanomaterials with a different type of dimension together, and the synergistic effect in the mixed-dimensional heterostructures will bring more opportunities to nanodevices.

It is known that the spatial resolution of conventional photodetectors is determined by device size and high spatial resolution can be accomplished by lithography technologies (28, 29). The conventional solution has also been used to tailor the in-plane geometry of the vdW photodetector for a higher spatial resolution (30). Note that the overlapping area of 2D materials determines the photosensitive area of a vdW heterostructure. This indicates that a method can be possibly developed to define a narrow photosensitive area by introducing a 1D nanomaterial into the stacking structure, since its 1D geometry can directly acquire an ultranarrow overlapping area. Here we show such a lithography-free technology route, which achieves an efficient electrical control on the spatial resolution of heterostructured photodetectors by introducing a 1D CNT into the vertically stacked architecture. The as-developed mixed-dimensional vdW heterostructure was composed of a CNT, WSe_2, and graphene, in which a WSe_2 flake was sandwiched between a metallic CNT and a graphene. WSe_2 was selected as the photoactive material, as it has high optical quality which has been demonstrated by light-emitting diodes (LEDs) as well as some optoelectronic devices (18, 31–33). Metallic CNT and graphene are the photocarrier collectors. It was demonstrated that the spatial resolution can be electrically controlled by tuning gate potentials (V_G) and drain-source bias voltages (V_{DS}) with the help of a scanning photocurrent microscopy (SPCM). Such a photodetector can work at both high-resolution mode (HRM) and low-resolution mode (LRM) with appropriate gate and bias voltages. The photosensitive area of the HRM and LRM was defined by the 1D CNT and the 2D graphene. Significantly, the HRM of the device was successfully applied to resolve the interference fringes with a period of 334 nm, validating the efficient electrical control. The mechanism for the electrical control properties can be ascribed to the

Significance

Spatial resolution can be electrically switched between high-resolution mode (HRM) and low-resolution mode in mixed-dimensional heterostructured photodetectors, and an interference fringe with 334 nm in period can be discriminated by setting at HRM. This can be attributed to the asymmetric geometry and the gate-tunable Fermi levels of these low-dimensional materials. It reveals great potential of the mixed-dimensional architectures in future nanoelectronics and nano-optoelectronics.

Author contributions: Ke Zhang, Y.W., and J.Z. designed research; Ke Zhang, H.M., X.Y., G.L., and Kenan Zhang performed research; Ke Zhang and Y.W. analyzed data; Ke Zhang, Y.W., Q.L., K.J., and S.F. wrote the paper; and Y.W. supervised the research.

The authors declare no conflict of interest.

This article is a PNAS Direct Submission.

[1]To whom correspondence should be addressed. Email: WeiYang@tsinghua.edu.cn.

This article contains supporting information online at www.pnas.org/lookup/suppl/doi:10.1073/pnas.1817229116/-/DCSupplemental.

Published online March 19, 2019.

asymmetric contacts from 1D CNT and 2D graphene and the unique band structure of the low-dimensional materials. The tunable spatial resolution demonstrates the distinctiveness of 1D/2D vdW heterostructures, which also reveals the combination of nanomaterials from multiple dimensions will bring diverse functions. Consequently, this progress opens up opportunities for mixed-dimensional architectures in future nanoelectronics and nano-optoelectronics.

Results

Fig. 1*A* sketches the CNT–WSe_2–graphene mixed-dimensional heterostructure. Fabrication procedures of the photodetector are schematically illustrated in *SI Appendix*, Fig. S1. Briefly, an individual metallic CNT, 1.19 nm in diameter (*SI Appendix*, Fig. S2), was pulled from a multiwalled carbon nanotube (MWCNT) and put onto a silicon wafer with a 300-nm SiO_2 layer (34). As the CNT is the inner shell of a MWCNT, it thus has a very clean surface and is suitable for the further vdW stacking with 2D materials. Mechanically exfoliated graphene was transferred onto a few-layer WSe_2 by a dry-transfer technique (35). The stacked WSe_2–graphene structure was then transferred onto the preset CNT. All of the transfer procedures were performed under an optical microscope equipped with precise manipulators. Ti/Au (10/50 nm) electrodes were electrically connected on the graphene, WSe_2, and CNT by electron beam lithography (EBL), electron beam evaporation, and lift-off procedures. To improve contacts, all of the devices were annealed at 350 °C in 400 mTorr Ar/H_2 ambient for 1 h. An as-fabricated device is shown in Fig. 1*C*, in which the CNT covered by the WSe_2 flake is indicated by a yellow dashed line. The CNT can be further confirmed by the *G* peak of the Raman spectrum as shown in Fig. 1*D*, *Inset* (36, 37), and the transfer curve of the CNT indicates that it is metallic (*SI Appendix*, Fig. S3). The multilayered WSe_2 is identified by the E^1_{2g} mode (248.585 cm^{-1}, in-plane mode), the A_{1g} mode (257.574 cm^{-1}, out-of-plane mode), and the B^1_{2g} mode (307.992 cm^{-1}, inactive mode), as shown in Fig. 1*D* (38). Its thickness is 5.21 nm, which is determined by atomic force microscope (AFM) (*SI Appendix*, Fig. S2). The *G* and *G′* peaks in Fig. 1*D*, *Inset* certify a multilayered graphene (39, 40) and the thickness is ∼3.56 nm.

Electrical transport properties of the as-fabricated heterostructures were studied under ambient conditions at room temperature. The graphene and the metallic CNT were set as source and drain electrodes via the Ti/Au terminals. A silicon wafer was used as the back gate to modulate the currents through the semiconducting WSe_2 channel. Transfer characteristics (I_{DS} vs. V_G) are plotted in Fig. 1*E*. The curves show that the device can be efficiently turned on/off by negative/positive gate voltages ($-/+V_G$). And the on/off ratio is about 10^4. This demonstrates that the WSe_2 channel in this vertical structure is p type, which is consistent with some recent reports on WSe_2 (4, 8). Moreover, the on current at positive drain-source bias ($+V_{DS}$) is much larger than that at negative bias ($-V_{DS}$), which can be ascribed to the asymmetric contacts on WSe_2 induced by the 2D graphene and 1D CNT. This can be further confirmed by the rectification effect indicated by the output curves (I_{DS} vs. V_{DS}; *SI Appendix*, Fig. S4). These asymmetric transport properties thus

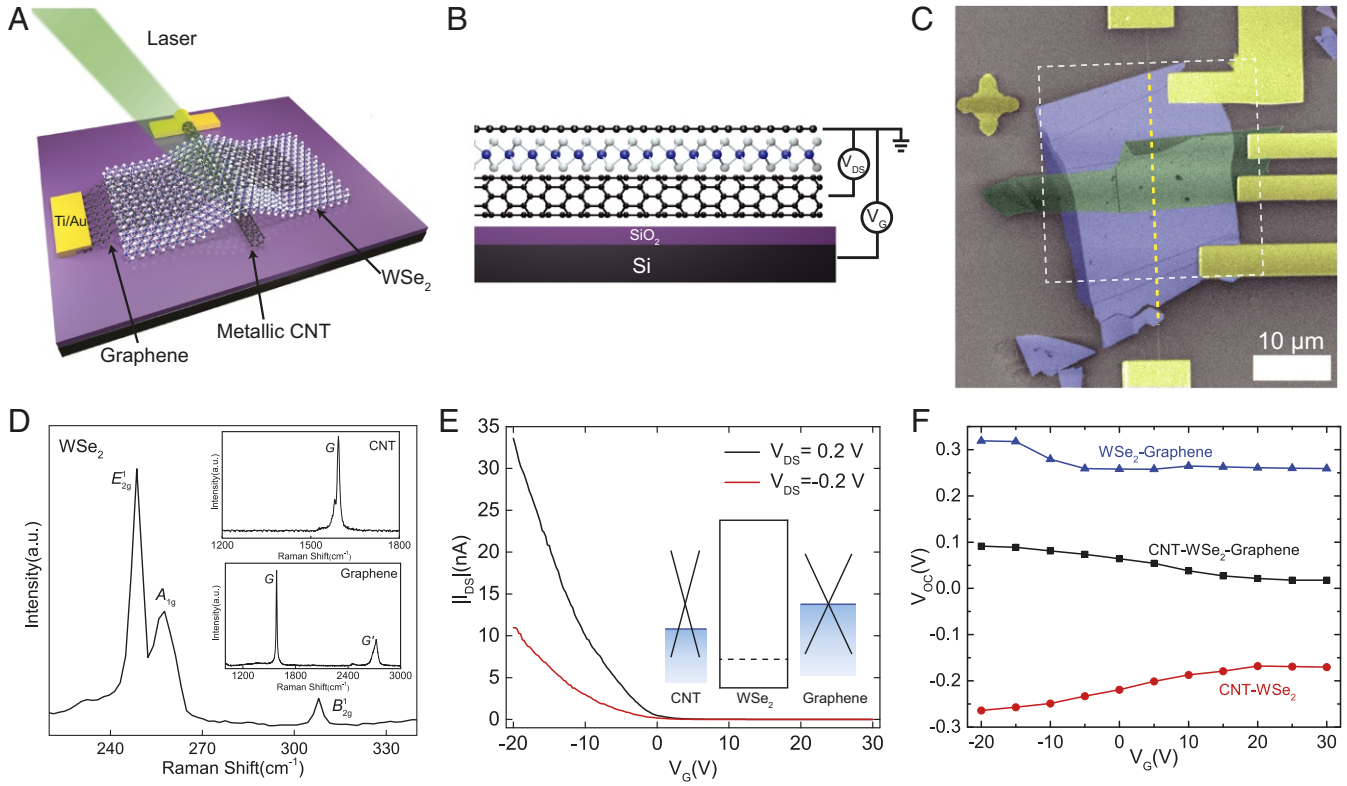

Fig. 1. CNT–WSe_2–graphene heterostructure and its properties. (*A*) Schematic illustration of the CNT–WSe_2–graphene heterostructure. (*B*) A cross-sectional view of the CNT–WSe_2–graphene heterostructure and the wiring diagram. Gate voltage is applied on the P^+ silicon. Drain-source bias is applied across the metallic CNT and graphene. (*C*) False color SEM image of a CNT–WSe_2–graphene heterostructure. The single metallic CNT is emphasized by the yellow dotted line, and the white square region indicates the scanning region of SPCM (Figs. 2*A* and 3*A*). (Scale bar: 10 μm.) (*D*) Raman spectroscopy of the WSe_2, CNT, and graphene in *C*, using a 532-nm laser. (*E*) Transfer characteristics of the heterostructure device at V_{DS} = ±0.2 V. *C*, *Inset* shows the relative Fermi levels of the three nanomaterials. (*F*) Open-circuit voltage (V_{OC}) as a function of gate voltage (V_G) under 24 μW, 520-nm laser illumination at CNT–WSe_2–graphene (black line), CNT–WSe_2 (red line), and WSe_2–graphene (blue line) areas.

show that the graphene's Fermi level is higher than the CNT's, as schematically illustrated in Fig. 1*E*, *Inset*.

The photoelectric properties were first investigated by SPCM. Fig. 2*A* is an SPCM image of the device in Fig. 1*C*, which was taken at $V_G = V_{DS} = 0$ V. The locations of the CNT, WSe_2, and graphene are also indicated by the dashed lines in the same image, revealing that the SPCM image fits well with the device geometry. In detail, photocurrents were generated in three different areas, dark blue, light blue, and red, which address the overlapping areas of CNT–WSe_2–graphene, WSe_2–graphene, and CNT–WSe_2. Moreover, the red and blue colors in the SPCM image correspond to the positive and negative photocurrents, respectively. It is known that photocurrent can be generated by charge separation induced by the built-in electric field at a metal–semiconductor contact. Thus, the CNT–WSe_2 contact and the WSe_2–graphene contact generate the positive (red) and negative (light blue) photocurrents. At the CNT–WSe_2 Schottky junction (red area), the photocurrents flow from the CNT to WSe_2, indicating that the direction of the built-in electric field is from CNT to WSe_2 as well. The light blue area suggests that at the WSe_2–graphene contact, the direction of the built-in electric field is from graphene to WSe_2. The Fermi level of CNT and graphene is thus higher than that of WSe_2. The built-in electric field at the CNT–WSe_2–graphene area is dominated by the two contacts for the ultrathin WSe_2 flake. Graphene's Fermi level is higher than CNT's for the negative photocurrents at this area, which agrees well with the results deduced from the electrical transport investigations. Therefore, the band diagram can be sketched as in Fig. 1*E*, *Inset*.

It is possible to reconfigure the photoelectric properties by electrical control methodology. Fig. 1*F* presents the V_G-dependent open-circuit voltage (V_{OC}) across the CNT and the graphene in the presence of focused laser beam illumination at the three typical areas, which are CNT–WSe_2, WSe_2–graphene, and CNT–WSe_2–graphene areas. Fig. 2 *B* and *C* shows the photocurrent mappings at variable V_G and V_{DS} by illuminating CNT–WSe_2 and WSe_2–graphene regions with the same focused laser beam, respectively. For the CNT–WSe_2 area, the device is more sensitive to the light illumination at both positive drain-source bias ($+V_{DS}$) and negative gate voltage ($-V_G$). At $+V_{DS}$, the direction of the external electric field is the same as that of the built-in electric field, so electron–hole pairs can be separated more efficiently. Furthermore, the device can provide larger photocurrents at $-V_G$, indicating a higher Schottky barrier at the CNT–WSe_2 interface. Negative gate potential induces the downshift of the Fermi levels of both the CNT and the WSe_2 layer. The higher Schottky barrier at $-V_G$ thus reveals that the gate potential has a more intensive impact on the WSe2's Fermi level than on the CNT's. This can be further confirmed by the higher V_{OC} at $-V_G$ as shown in Fig. 1*F*. The corresponding band alignments at the CNT–WSe_2 interface can be found in Fig. 2*E*. In the case of the WSe_2–graphene area, the built-in electric field is opposite to that at the CNT–WSe_2 interface, and the Fermi level of multilayered graphene is relatively difficult to modulate for its higher density of state at the Dirac cone and the electrostatic screening effect induced by the WSe_2 underlayer, so the photocurrent becomes prominent at $-V_{DS}$ and $-V_G$ (Fig. 2*C* and *SI Appendix*, Fig. S5). By comparing Fig. 2 *B* and *C*, it can be found that the photoelectric properties at CNT–WSe_2 and WSe_2–graphene areas are apparently different, validating the reconfigurable photoelectric properties of such mixed-dimensional devices by electrical control.

The electrical control effect on localized areas suggests that it is necessary to further explore the photosensitive area of the device at different V_{DS} and V_G by SPCM. The representative 3×3 SPCM images are presented in Fig. 3*A*, in which V_{DS} is varied from -0.2 V to 0.2 V with a step of 0.2 V and V_G is set as -20 V, 0 V, and +30 V, respectively. From these SPCM images, it can be found that the CNT looks clear in Fig. 3*A*, *Top Left* and

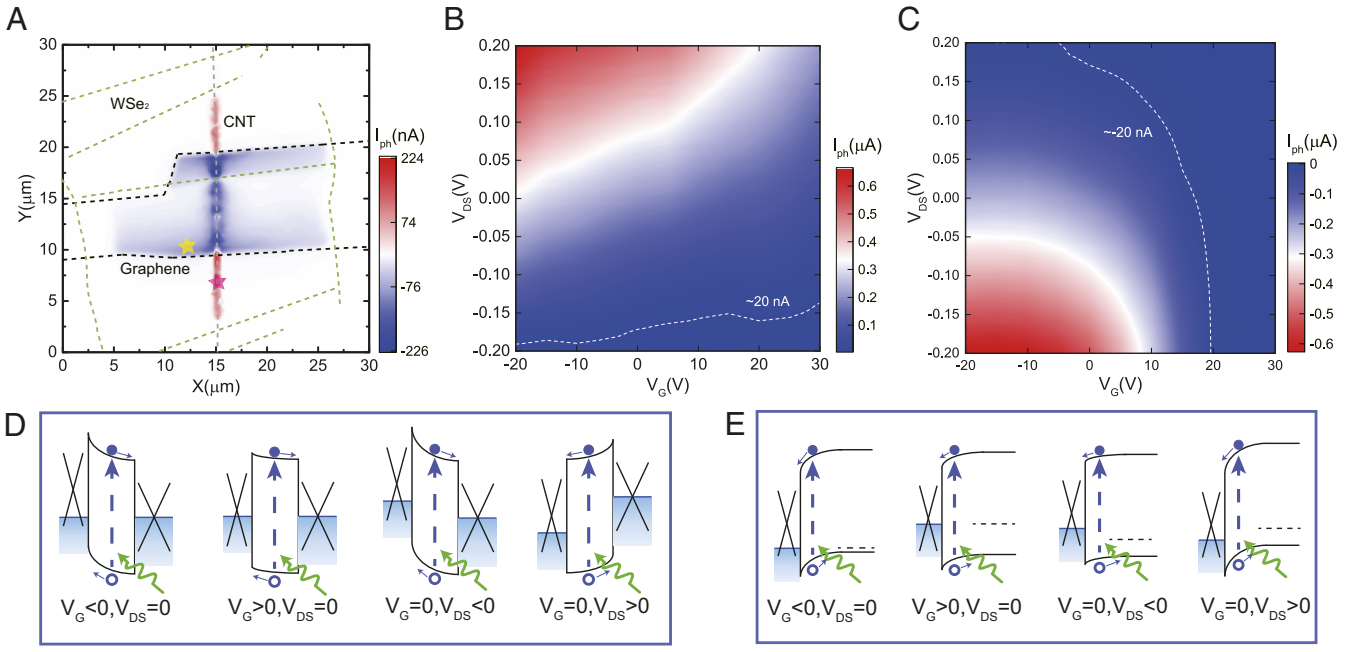

Fig. 2. Spatial-resolved and electrical-bias–dependent photocurrent generation and the corresponding band diagrams. (*A*) A representative SPCM image of the heterostructure device taken at $V_G = V_{DS} = 0$ V (laser wavelength, 520 nm; power, 24 μW; spot size, ∼1 μm). Black and green dashed lines indicate the edges (or cracks) of the graphene and WSe_2, respectively, and the gray dashed line indicates the position of the CNT. Scanning area: 30 μm × 30 μm. (*B* and *C*) V_G- and V_{DS}-dependent photocurrent mappings of CNT–WSe_2 (*B*) and WSe_2–graphene (*C*) regions with laser spot illuminating at the pink star and yellow star shown in *A*. Contour lines of 20 nA (*B*) and −20 nA (*C*) are marked by white dashed lines, where the CNT–WSe_2/WSe_2–graphene area becomes illumination insensitive. (*D* and *E*) Band diagrams of CNT–WSe_2–graphene (*D*) and CNT–WSe_2 (*E*) at different electrical biases.

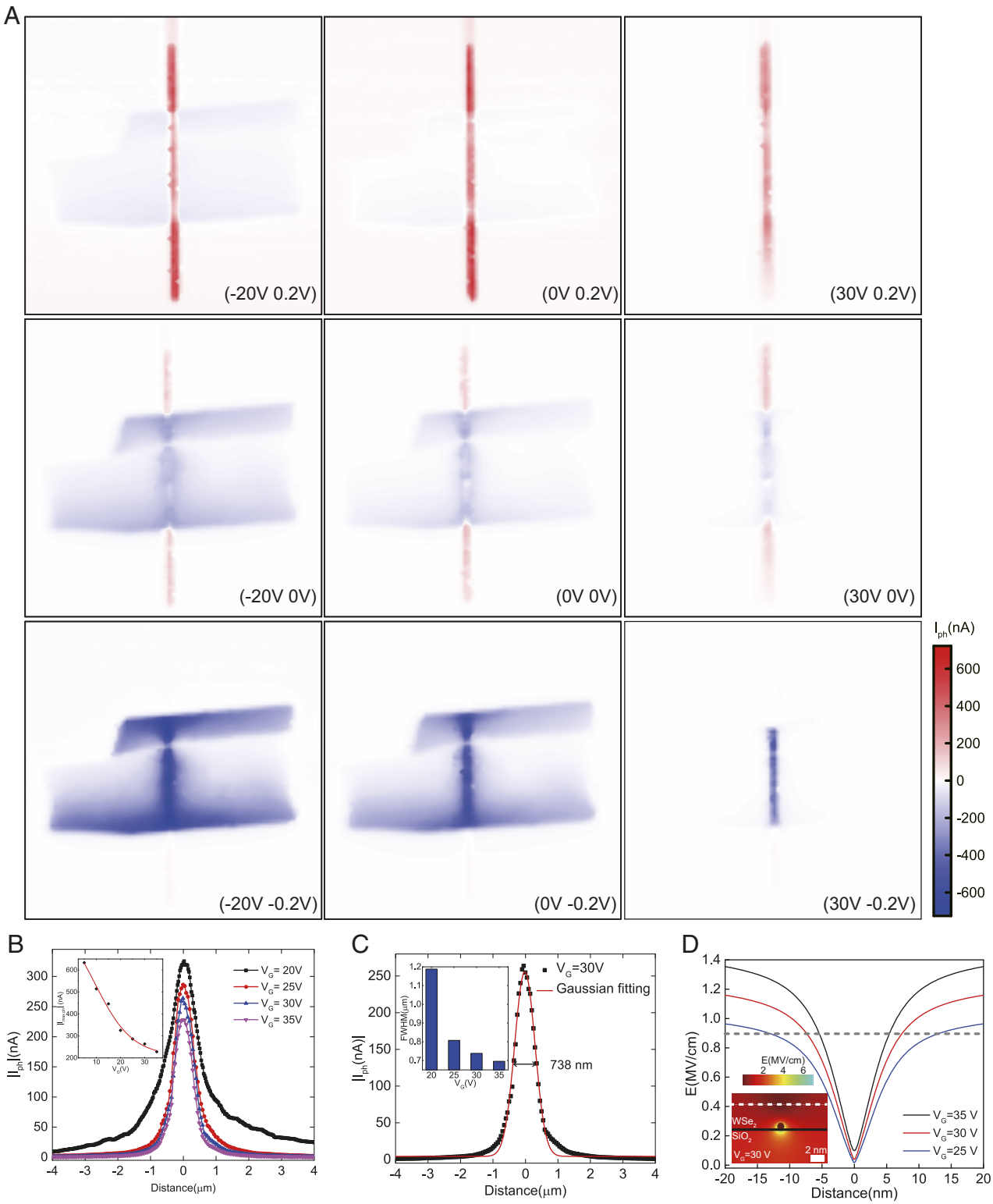

Fig. 3. Electrical control on the photosensitive area of the device via modulating V_G and V_{DS}. (*A*) SPCM images with V_{DS} varied from −0.2 V to 0.2 V with a step of 0.2 V and V_G set as −20 V, 0 V, and +30 V, respectively. Scanning area: 30 μm × 30 μm. (*B*) Photocurrent distributions along the direction perpendicular to the CNT at V_{DS} = −0.2 V. (*B*, *Inset*) Relationship between maximum photocurrents and gate voltages. (*C*) Gaussian fitting of photocurrent at V_G = 30 V and V_{DS} = −0.2 V. FWHM derived from the fitting curve is 738 nm. (*C*, *Inset*) FWHM at various V_G. (*D*) Simulated electric-field intensity distribution along the white dashed line in *Inset* at V_{DS} = −0.2 V and V_G = 25 V, 30 V, and 35 V.

the graphene becomes clear in Fig. 3*A*, *Bottom Left*. Moreover, varying V_{DS} and V_G can gradually modulate the SPCM images. These phenomena agree well with the position of the "hot spots" (the red areas in Fig. 2 *B* and *C*) and the variation tendency of photocurrents in Fig. 2 *B* and *C*. The SPCM images further indicate that the device has two working modes. The first one

is LRM (Fig. 3*A*, *Bottom Left*). The whole overlapping region of WSe_2 and graphene has a prominent response to illumination and the photocurrents flow along the same direction in the whole photosensitive area. As the photosensitive area of LRM is much larger than the spot size of the focused laser beam, the spatial resolution in this case could be determined by the overlapped WSe_2 and graphene, typically several tens of micrometers in size. The second one is HRM (Fig. 3*A*, *Bottom Right*). Only overlapping the area of the three materials has a photoresponse. The CNT–WSe_2 area is invisible in both modes for that negative bias potential strongly decreases the band bending in WSe_2 and the positive gate potential could drastically decrease the Fermi-level difference between CNT and WSe_2. The two factors reduce the band bending at the CNT–WSe_2 interface and thus reduce electron–hole separation and photocurrent generation at this area. The absence of the WSe_2–graphene area in the HRM SPCM image can be ascribed to the reduced band bending induced by positive V_G. High positive gate voltage increases the Fermi level of WSe_2 and reduced the built-in electric field dramatically. Weak photocurrents at the WSe_2–graphene area can be ensured at relatively weak $-V_{DS}$. Furthermore, experiments revealed that the HRM is more sensitive to the electric bias, and it is time consuming to define the proper parameters for HRMs. Fig. 2 *B* and *C* provides an efficient method. Typically, the area in an SPCM image becomes very light and even invisible when the photocurrents of this area are below 20 nA, since the photocurrents at the hot spots are over several hundred nanoamps. Contour lines of 20 nA and −20 nA were thus plotted in Fig. 2 *B* and *C* to mark the critical electrical parameters, at which the CNT–WSe_2 and WSe_2–graphene areas become illumination insensitive. By overlapping Fig. 2 *B* and *C*, the two contour lines will cross and divide the (V_G, V_{DS}) coordinate system into four parts (*SI Appendix*, Fig. S6). In *SI Appendix*, Fig. S6 the bottom right part shows the appropriate parameters for HRM, since such a biased device has a weak photocurrent output at CNT–WSe_2 and WSe_2–graphene areas and thus the two areas will be absent in the SPCM image. The LRMs and HRMs revealed by SPCM studies further confirm the electrical control on photoelectric properties, and the tunable spatial resolution should be due to the asymmetric contacts on the semiconducting WSe_2 from the 1D CNT and the 2D graphene.

More experiments were further carried out to study the V_G-dependent photocurrent distribution at HRM. The focused laser beam was used to scan the photosensitive area at HRM with a much smaller step, and Fig. 3*B* plots the photocurrent distributions along the direction vertical to the CNT. The curves reveal that photocurrent distribution of the device can be modulated by gate potential, and narrower distribution can be accomplished by increasing positive gate potential (Fig. 3*C*, *Inset*). Numerically, Gaussian fitting shows the full width at half maximum (FWHM) is 738 nm for V_G = 30 V and V_{DS} = −0.2 V (Fig. 3*C*). The spot size of the focused laser beam is ≈700 nm, which is calculated by 1.22 λ/N.A., where $\lambda = 520$ nm and the numerical aperture is 0.9. The FWHM and the spot size are very close, revealing that the HRM has such a high spatial resolution that it can be used to profile the focused laser spot. This feature benefits from the 1D CNT with less than 2 nm diameter. The small CNT makes the overlapping area ultranarrow and the electric field introduced by biasing CNT is also localized in the nanoscale range (25). However, the accurate measurement of the spatial resolution of HRM is a challenge, which could be possibly addressed by developing specific near-field optics methodology for the device (41). Gaussian fitting also revealed that the main peak fits well except the edge of the peak. The deviation can possibly be ascribed to the screening effect of the CNT at HRM. Electric-field simulation was thus performed and the results are presented in Fig. 3*D*. The shadow above the CNT in Fig. 3*D*, *Inset* indicates lower electric-field strength, validating the CNT-induced localized screening effect on the WSe_2. The screening effect reduces the modulation efficiency of the gate electrode, inducing a broadening photosensitive area. Furthermore, the tunable spatial resolution at HRM can also be attributed to the screening effect. Fig. 3*D* plots the distribution of electric-field intensity above the CNT, which reveals that a higher gate voltage could induce a narrower screening area and a higher spatial resolution (Fig. 3*B* and Fig. 3*C*, *Inset*). In addition, it is able to modulate the photocurrent at the CNT–WSe_2–graphene area by gate voltage (Fig. 3*B*, *Inset*), since the photocurrent generation is dominated by the Fermi-level difference between CNT and graphene, which can be tuned by the gate potential. As sketched in Fig. 1*E*, *Inset*, the Fermi level of the CNT is slightly lower than that of graphene, so the photocurrent output at $-V_G$ is larger than at $+V_G$. This can also be confirmed by the V_G-dependent V_{OC} as plotted in Fig. 1*F*. All these results further reveal the electrical control properties of the as-developed mixed-dimensional heterostructures, which will be promising photodetectors.

The photoelectric output properties were further investigated. A defocused laser spot, 10 μm in diameter, was used to illuminate the CNT–WSe_2–graphene overlapping area with different output powers. Output curves at varying incident laser power were plotted at V_G = 30 V (Fig. 4*A*) and V_G = −20 V (Fig. 4*B*), respectively. From Fig. 4 *A* and *B*, it can be found that the device has a photovoltaic output, since the output curves deviate from the point of origin under light illumination, which is determined

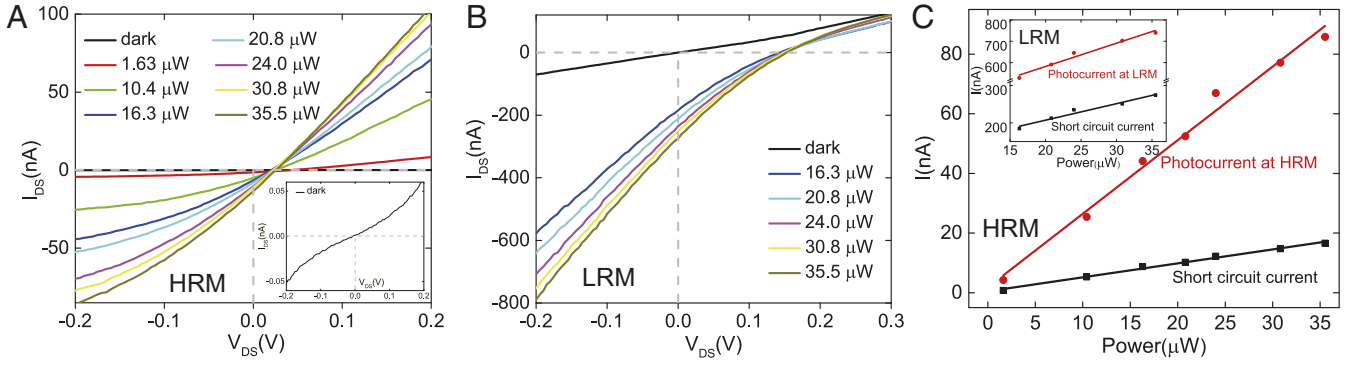

Fig. 4. Photoelectric output properties of the heterostructure device. (*A* and *B*) Output characteristics (I_{DS} vs. V_{DS}) at HRM (V_G = 30 V and V_{DS} = −0.2 V, *A*) and LRM (V_G = −20 V and V_{DS} = −0.2 V, *B*) with a laser beam (wavelength, 520 nm; spot size, 10 μm) illuminating the CNT–WSe_2–graphene area. *A*, *Inset* plots the dark currents. (*C*) Photocurrents at HRM (V_G = 30 V and V_{DS} = −0.2 V) and LRM (V_G = −20 V and V_{DS} = −0.2 V, *Inset*) and short-circuit currents at V_G = 30 V and V_G = −20 V (*Inset*) as a function of laser power. Black and red lines are the linear fitting of the experimental data.

by the asymmetric contacts on WSe_2. The output curves further reveal that the open-circuit voltage was nearly independent of the laser power, whereas the short-circuit current (I_{SC}) was found to increase linearly with incident power intensity (Fig. 4*C* for HRM and Fig. 4*C*, *Inset* for LRM), as more photoinduced electron–hole pairs will be separated and contribute to a higher I_{SC}. The photocurrent at HRM (V_G = 30 V, V_{DS} = −0.2 V) and LRM (V_G = −20 V, V_{DS} = −0.2 V) can also be obtained from the output curves (Fig. 4*C* and Fig. 4*C*, *Inset*), and it is linear to the laser power. The responsivity can thus be calculated from slopes of linear fitting. The as-calculated responsivities of HRM and LRM are 2.47 mA/W and 10.9 mA/W, respectively. Note that it is a conservative estimate on the HRM. The photosensitive area is defined by the CNT, which is nanoscaled and much smaller than the light spot. It is still a challenge to determine the exact photosensitive area at HRM, although it can be possibly measured by scanning probe microscopy (SPM) methodology. Hence, the light power illuminated on the actual photosensitive area is overestimated, leading to a conservative estimate on the responsivity. Even so, it is still superior to some previous works (42). It is known that vacancies and impurities in WSe_2 could introduce traps and recombination centers for photocarriers, which have significant impact on the lifetime of photocarriers as well as the photocurrent output. Thus, the responsivity could be further modulated by the improvements of materials and structures (43, 44).

The high spatial resolution achieved by electrical control is prospective in practical applications. It is known that spatial resolution of photodetectors is very important for spectral detection. Further experiments were performed to explore the potential of the HRM in spectral measurements. A green laser beam ($\lambda = 520$ nm) was split by a transmission grating and then focused by a cylindrical lens, as sketched in Fig. 5*A*. Fig. 5*A*, *Bottom* is an image on a viewing screen at the focal plane, in which bright stripes from 0, ±1, ±2 orders can be identified. To plot the intensity distribution of the stripes, an as-fabricated device setting at HRM was used to linearly sweep the stripes on the focal plane. The photocurrents were plotted as a function of the location, which is shown in Fig. 5*B* and Fig. 5*B*, *Inset*. All of the peaks from the brightest (1 order) to the weakest (0 order) can be resolved clearly in the curves. The signal-to-noise ratio (SNR) exceeds ∼5,000, which is defined as I_{ph}/I_n, where I_{ph} is the maximum photocurrent captured by the device and I_n is the noise level of the working mode. These results preliminarily show its potential in spatial-resolved light detection. Moreover, the device will be unique and more powerful in fine spectral structure, since it has a nanoscaled spatial resolution, which is determined by the mixed-dimensional architecture and has been validated in the SPCM studies. The device was thus used to evaluate the spatial distribution of a double-beam interference system ($\lambda = 343$ nm, Fig. 5*C*). Here a lock-in amplifier was used to measure the photocurrents, and more details can be found in *Materials and Methods*. The device linearly scanned at the interference region as sketched in Fig. 5*C*, and the spatial-resolved distribution is successfully plotted in Fig. 5*D*. The period is calculated to be 340.5 nm by cosine function fitting. Based on the classical optical theory, distribution of light intensity for the double-beam interference system is $I = 2I_0(1 + \cos(2kx \sin\theta))$, in which λ = 343 nm and $\theta = 30°$. The interference fringes distribution thus follows cosine function with a period of 343 nm. The experimental distribution fits well with this principle. The optical system is widely used to fabricate 1D grating structure. Fig. 5*C*, *Inset* shows such a grating structure on a quartz substrate with 334 nm in period. The period derived from the spatial-resolved distribution coincides with the period obtained from SEM images with no more than 1.95% error. All of the above investigations show that the as-developed devices have great potential in spectrum detection.

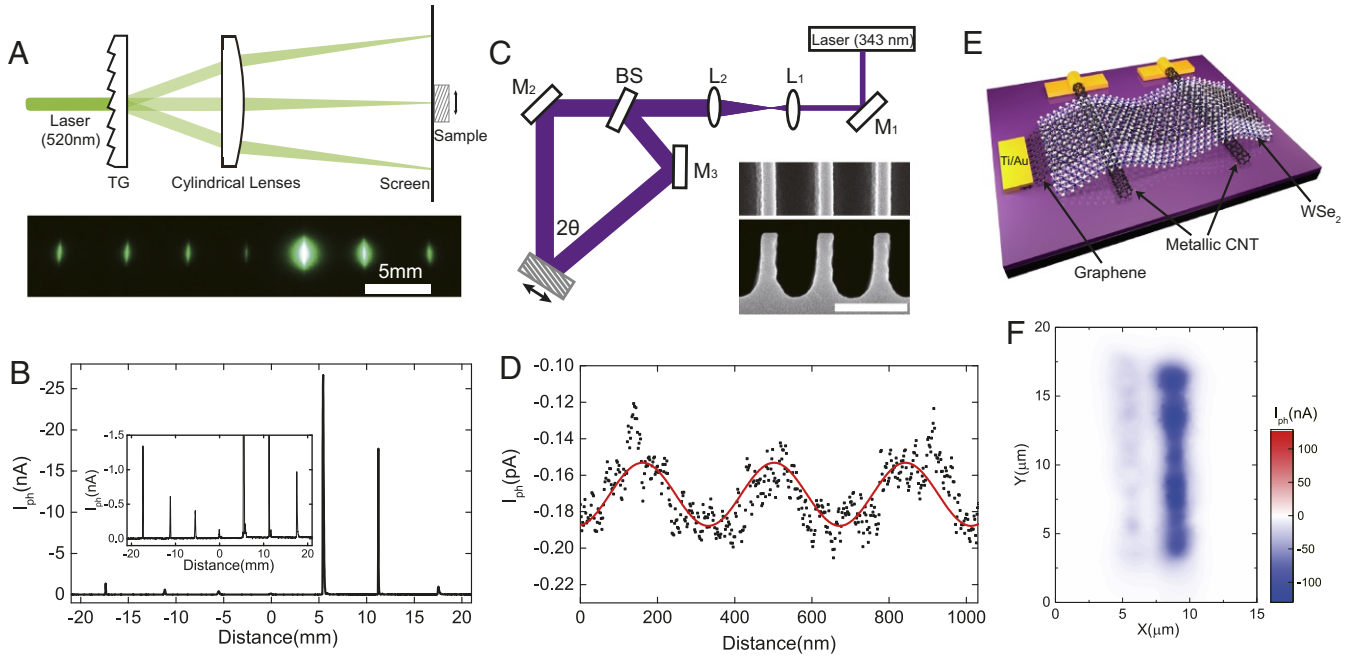

Fig. 5. Examples of photodetection and integration. (*A*) Detection of the light distribution from a grating splitter irradiated by a green laser beam ($\lambda = 520$ nm). *Top* sketches the optical path diagram. *Bottom* is an optical image taken on a viewing screen, in which the fringe spacing is ∼5.82 mm. (*B*) Photocurrent intensity distribution plotted by the photodetector setting at HRM (V_G = 30 V, V_{DS} = −0.2 V) on the focal plane. (*C*) Schematic of a double-beam interference system ($\lambda = 343$ nm). Laser power and spot size were 4.8 mW and 1.5 cm, respectively. *C*, *Inset* presents SEM images of a grating, 334 nm in period, fabricated by the interference system. (Scale bar: 250 nm.) (*D*) Spatial-resolved light distribution of the interference fringes plotted by the device setting at HRM (V_G = 30 V, V_{DS} = −0.2 V). Sine fitting shows the period is 340.5 nm. (*E*) Schematic illustration of an integration solution with two parallel metallic CNTs. (*F*) A representative SPCM image of an as-sketched device biasing at HRM (V_G = 30 V, V_{DS} = −0.2 V), in which the two CNTs can be clearly distinguished from each other.

Integration of the mixed-dimensional heterostructures is also an important issue for practical applications. Horizontally aligned carbon nanotube arrays can be grown on large-scale wafers by chemical vapor deposition (CVD) techniques (45, 46). It is thus possible to make a linear integration by using parallel metallic CNTs as the bottom electrodes. To show this probability, two metallic CNTs were used to build a 1×2 architecture (Fig. 5*E*). Two parallel CNTs were put onto a Si/SiO_2 wafer with a spacing of ~3.3 μm. The thicknesses of WSe_2 and graphene covered on CNTs are 31.29 nm and 2.72 nm, respectively (*SI Appendix*, Fig. S7). The SPCM investigations verified that the two CNTs can be clearly distinguished from each other, when the devices were set at HRM (V_G = 30 V, V_{DS} = −0.2 V), as shown in Fig. 5*F*. The tunable spatial resolution makes the integrated device workable, since the electric bias can restrict the photosensitive area around the CNT electrode and the two neighboring devices can thus be discriminated even if they are not physically separated. The difference of photocurrent intensity between the two sensitive areas originated from the different diameters of the two CNTs (*SI Appendix*, Fig. S7). A linear array thus can be possibly achieved by scaling up the strategy with the development on the controllable growth of CNTs on diameter and chirality as well as the controllable growth of 2D materials.

More heterostructures can be derived from the CNT–WSe_2–graphene structure, in which a semiconducting 2D flake is asymmetrically sandwiched between a 1D electrode and a 2D graphene. A Ti/Au nanowire–WSe_2–graphene device was thus fabricated to demonstrate this issue. The details can be found in *SI Appendix*, Fig. S8. The Ti/Au nanowire, which is 370 nm in width and 30 nm in thickness, was fabricated by EBL, electron beam evaporation, and lift-off procedures. Other fabrication procedures were the same as for the CNT–WSe_2–graphene devices. Thicknesses of WSe_2 and graphene are 8.85 nm and 7.02 nm, respectively. The SPCM observations (*SI Appendix*, Fig. S8*D*) revealed that the device behaves in a similar way. It also has an HRM ($V_G > 0$ and $V_{DS} < 0$) and an LRM ($V_G < 0$ and $V_{DS} < 0$). Moreover, the LRM is apparently different from that for the CNT–WSe_2–graphene devices, since the WSe_2–graphene region in the LRM SPCM image is much weaker. This can be ascribed to the Ti/Au nanowire, as its Fermi level can hardly be tuned by the gate potential. The difference can further validate the uniqueness of the CNT electrode in such a heterostructure. In addition, the sandwiched 2D semiconductor also has many options, such as black phosphorus (BP). Compared with the indirect bandgap of multilayered transition metal dichalcogenides, BP is a direct-bandgap semiconductor, suggesting that BP has a good photoelectric conversion efficiency. Furthermore, BP has a proper bandgap for near-infrared photodetection (47).

Discussion

A vertically staked CNT–WSe_2–graphene architecture was proposed and fabricated to explore the potential of such a mixed-dimensional heterostructure as high-performance photodetectors. In addition to the 2D photosensitive WSe_2, the two contacts were also carefully selected, which were the 1D CNT and the 2D graphene. The asymmetrical configuration endows the device with a distinctive electrical control property on spatial resolution. SPCM observations revealed that photosensitive areas are sensitive to both gate and drain-source bias potentials and two working modes (LRM and HRM) can be achieved via appropriate electrical bias. The reconfigurable spatial resolution can be attributed to the gate-tunable Fermi levels of the low-dimensional materials, following the tunable built-in electric field of the interfacial Schottky barriers. The overlapping areas of CNT–WSe_2–graphene, WSe_2–graphene, and CNT–WSe_2 can thus serve as photosensitive areas by electrical control, respectively. The device works at HRM by biasing the device at $+V_G$ and $-V_{DS}$, and the overlapping area of CNT–WSe_2–graphene is the photosensitive area in this case. The LRM can be realized by $-V_G$ and $-V_{DS}$. Moreover, interference fringes with 334 nm period were successfully discriminated by the device working at HRM, revealing the spatial-resolving power. These results not only validate the efficiency of electrical control on the as-developed mixed-dimensional heterostructures, making the device function reconfigurable, but also derive a lithography-free technology to achieve high spatial resolution with vdW heterostructures. The 1D/2D mixed-dimensional architectures are promising for future nanoelectronics and nano-optoelectronics, since more reconfigurable functions can possibly be realized via the electrical control methodology on the basis of the diverse low-dimensional nanomaterials.

Materials and Methods

Fabrication of the Metallic CNT–WSe_2–Graphene Heterostructure. To fabricate the vertical metallic CNT–WSe_2–graphene devices, MWCNTs (usually double or triple walled) were grown on silicon substrate with trenches of several hundred micrometers by the chemical vapor transport method. Some TiO_2 nanoparticles were deposited onto the suspended parts of the CNTs for visualization (34). With an optical microscope (Olympus BX51M) and two homemade tips, we cut and take off the outer shell of the suspended part of a single CNT, maintaining the inner part, which is ultraclean. A WSe_2 single crystal was grown via the chemical vapor transport method. Few-layered sheets of WSe_2 (graphene) were mechanically exfoliated from a bulk and then identified by optical contrast and Raman spectroscopy. Heterostructures were assembled using the dry transfer method with a transfer slide composed of a stack of glass, a polymer [polydimethylsiloxane (PDMS)], and a carrier layer [polyvinyl alcohol (PVA)]. Electrical contacts to the three typical materials' electrodes are patterned using electron-beam lithography followed by evaporation of 10 nm Ti/50 nm Au.

Microscopy and Electrical Measurements. SEM images were obtained on FEI Nova NanoSEM 450 with operating voltage at 1 kV. Atomic force microscopy (AFM) images were carried out in tapping mode. Raman spectroscopies were acquired with 1 μm spot size and 532 nm wavelength. Electrical measurements were carried out on a Lakeshore CRX-4K in vacuum.

Scanning Photocurrent Microscopy. A focused 520-nm laser beam was used to illuminate the surface of the device through a 100× objective lens with numerical aperture of 0.9. The spot size was ~1 μm. A 2D piezoelectric stage was used to drive the device to move around the focused laser beam. Gate and bias voltages were applied from an Agilent B2902A, which can also measure the corresponding current. With the device scanning around the laser spot, photocurrent is recorded as a function of the device location, and all of the processes are controlled by a homemade program. To improve the signal-to-noise ratio, a lock-in amplifier (SR810) and a current preamplifier (SR570) were used to collect photocurrent and an Agilent B2902A was used to apply voltages.

ACKNOWLEDGMENTS. This work was financially supported by the National Key Research and Development Program of China (Grant 2018YFA0208401), the National Natural Science Foundation of China (Grant 61774090), the National Key Research and Development Program of China (Grant 2017YFA0205800), the National Natural Science Foundation of China (Grants 51472142 and 51727805), and Beijing Natural Science Foundation (Grant 2184099).

1. Geim AK, Grigorieva IV (2013) Van der Waals heterostructures. *Nature* 499: 419–425.
2. Britnell L, et al. (2012) Field-effect tunneling transistor based on vertical graphene heterostructures. *Science* 335:947–950.
3. Jong Yu W, et al. (2012) Vertically stacked multi-heterostructures of layered materials for logic transistors and complementary inverters. *Nat Mater* 12:246–252.
4. Cheng R, et al. (2014) Electroluminescence and photocurrent generation from atomically sharp WSe_2/MoS_2 heterojunction p-n diodes. *Nano Lett* 14:5590–5597.
5. Zhang J, et al. (2017) Carbon-nanotube-confined vertical heterostructures with asymmetric contacts. *Adv Mater* 29:1702942.
6. Xia F, Wang H, Xiao Di, Dubey M, Ramasubramaniam A (2014) Two-dimensional material nanophotonics. *Nat Photon* 8:899–907.

7. Koppens FHL, et al. (2014) Photodetectors based on graphene, other two-dimensional materials and hybrid systems. *Nat Nanotechnol* 9:780–793.
8. Zhou X, et al. (2018) Tunneling diode based on WSe_2/SnS_2 heterostructure incorporating high detectivity and responsivity. *Adv Mater* 30:1703286.
9. Barati F, et al. (2017) Hot carrier-enhanced interlayer electron–hole pair multiplication in 2D semiconductor heterostructure photocells. *Nat Nanotechnol* 12:1134–1139.
10. Hong X, et al. (2014) Ultrafast charge transfer in atomically thin MoS_2/WS_2 heterostructures. *Nat Nanotechnol* 9:682–686.
11. Baugher BWH, Churchill HOH, Yang Y, Jarillo-Herrero P (2014) Optoelectronic devices based on electrically tunable p–n diodes in a monolayer dichalcogenide. *Nat Nanotechnol* 9:262–267.
12. Barkelid M, Zwiller V (2014) Photocurrent generation in semiconducting and metallic carbon nanotubes. *Nat Photon* 8:47–51.
13. Rivera P, et al. (2015) Observation of long-lived interlayer excitons in monolayer $MoSe_2$–WSe_2 heterostructures. *Nat Commun* 6:6242.
14. Furchi MM, Pospischil A, Libisch F, Burgdorfer J, Mueller T (2014) Photovoltaic effect in an electrically tunable van der Waals heterojunction. *Nano Lett* 14:4785–4791.
15. Liu Y, et al. (2015) Toward barrier free contact to molybdenum disulfide using graphene electrodes. *Nano Lett* 15:3030–3034.
16. Britnell L, et al. (2013) Strong light-matter interactions in heterostructures of atomically thin films. *Science* 340:1311–1314.
17. Jong Yu W, et al. (2013) Highly efficient gate-tunable photocurrent generation in vertical heterostructures of layered materials. *Nat Nanotechnol* 8:952–958.
18. Massicotte M, et al. (2016) Picosecond photoresponse in van der Waals heterostructures. *Nat Nanotechnol* 11:42–46.
19. Lee C-H, et al. (2014) Atomically thin p–n junctions with van der Waals heterointerfaces. *Nat Nanotechnol* 9:676–681.
20. Roy T, et al. (2014) Field-effect transistors built from all two-dimensional material components. *ACS Nano* 8:6259–6264.
21. Lee G-H, et al. (2013) Flexible and transparent MoS_2 field-effect transistors on hexagonal boron nitride-graphene heterostructures. *ACS Nano* 7:7931–7936.
22. Liu C, et al. (2018) A semi-floating gate memory based on van der Waals heterostructures for quasi-non-volatile applications. *Nat Nanotechnol* 13:404–410.
23. Li D, et al. (2017) Two-dimensional non-volatile programmable p–n junctions. *Nat Nanotechnol* 12:901–906.
24. Choi MS, et al. (2013) Controlled charge trapping by molybdenum disulphide and graphene in ultrathin heterostructured memory devices. *Nat Commun* 4:1624.
25. Desai SB, et al. (2016) MoS_2 transistors with 1-nanometer gate lengths. *Science* 354:99–102.
26. Qiu C, et al. (2017) Scaling carbon nanotube complementary transistors to 5-nm gate lengths. *Science* 355:271–276.
27. Zhang J, et al. (2017) SWCNT-MoS_2-SWCNT vertical point heterostructures. *Adv Mater* 29:1604469.
28. Li W-D, Chou SY (2010) Solar-blind deep-UV band-pass filter (250-350 nm) consisting of a metal nano-grid fabricated by nanoimprint lithography. *Opt Express* 18: 931–937.
29. Yu Z, Schablitsky SJ, Chou SY (1999) Nanoscale GaAs metal–semiconductor–metal photodetectors fabricated using nanoimprint lithography. *Appl Phys Lett* 74:2381–2383.
30. Xie L, et al. (2017) Graphene-contacted ultrashort channel monolayer MoS_2 transistors. *Adv Mater* 29:1702522.
31. Ross JS, et al. (2014) Electrically tunable excitonic light-emitting diodes based on monolayer WSe_2 p–n junctions. *Nat Nanotechnol* 9:268–272.
32. Jones AM, et al. (2013) Optical generation of excitonic valley coherence in monolayer WSe_2. *Nat Nanotechnol* 8:634–638.
33. Zhao W, et al. (2012) Evolution of electronic structure in atomically thin sheets of WS_2 and WSe_2. *ACS Nano* 7:791–797.
34. Deng G-W, et al. (2016) Strongly coupled nanotube electromechanical resonators. *Nano Lett* 16:5456–5462.
35. Castellanos-Gomez A, et al. (2014) Deterministic transfer of two-dimensional materials by all-dry viscoelastic stamping. *2D Mater* 1:011002.
36. Dresselhaus MS, Dresselhaus G, Saito R, Jorio A (2005) Raman spectroscopy of carbon nanotubes. *Phys Rep* 409:47–99.
37. H Hiura, TW Ebbesen, K Tanigaki, H Takahashi (1993) Raman studies of carbon nanotubes. *Chem Phys Lett* 202:509–512.
38. Tonndorf P, et al. (2013) Photoluminescence emission and Raman response of monolayer MoS_2, $MoSe_2$, and WSe_2. *Opt Express* 21:4908–4916.
39. Ferrari AC, et al. (2006) Raman spectrum of graphene and graphene layers. *Phys Rev Lett* 97:187401.
40. Ni Z, Wang Y, Yu T, Shen Z (2008) Raman spectroscopy and imaging of graphene. *Nano Res* 1:273–291.
41. Rauhut N, et al. (2012) Antenna-enhanced photocurrent microscopy on single-walled carbon nanotubes at 30 nm resolution. *ACS Nano* 6:6416–6421.
42. Groenendijk DJ, et al. (2014) Photovoltaic and photothermoelectric effect in a double-gated WSe_2 device. *Nano Lett* 14:5846–5852.
43. Klots AR, et al. (2014) Probing excitonic states in suspended two-dimensional semiconductors by photocurrent spectroscopy. *Sci Rep* 4:6608.
44. Anh Nguyen D, et al. (2018) Highly enhanced photoresponsivity of a monolayer WSe_2 photodetector with nitrogen-doped graphene quantum dots. *ACS Appl Mater Inter* 10:10322–10329.
45. Kang SJ, et al. (2007) High-performance electronics using dense, perfectly aligned arrays of single-walled carbon nanotubes. *Nat Nanotechnol* 2:230–236.
46. Ding L, Yuan D, Liu J (2008) Growth of high-density parallel arrays of long single-walled carbon nanotubes on quartz substrates. *J Am Chem Soc* 130:5428–5429.
47. Guo Q, et al. (2016) Black phosphorus mid-infrared photodetectors with high gain. *Nano Lett* 16:4648–4655.